Journal of Alloys and Compounds 781 (2019) 734–743

Contents lists available at ScienceDirect

Journal of Alloys and Compounds

journal homepage: http://www.elsevier.com/locate/jalcom

On the mechanism of extraordinary strain hardening in an interstitial high-entropy alloy under cryogenic conditions

Zhangwei Wang*, Wenjun Lu, Dierk Raabe, Zhiming Li**

Max-Planck-Institut für Eisenforschung, Max-Planck-Str. 1, 40237, Düsseldorf, Germany

ARTICLE INFO

Article history:
Received 19 October 2018
Received in revised form
2 December 2018
Accepted 4 December 2018
Available online 6 December 2018

Keywords:
Interstitial high-entropy alloy
Phase transformation
Stacking fault
Mechanical properties
Strain hardening

ABSTRACT

We investigate the cryogenic deformation response and underlying mechanisms of a carbon-doped interstitial high-entropy alloy (iHEA) with a nominal composition of $Fe_{49.5}Mn_{30}Co_{10}Cr_{10}C_{0.5}$ (at. %). Extraordinary strain hardening of the iHEA at 77 K leads to a substantial increase in ultimate tensile strength (~1300 MPa) with excellent ductility (~50%) compared to that at room temperature. Prior to loading, iHEAs with coarse (~100 μm) and fine (~6 μm) grain sizes show nearly single face-centered cubic (FCC) structure, while the fraction of hexagonal close-packed (HCP) phase reaches up to ~70% in the cryogenically tensile-fractured iHEAs. Such an unusually high fraction of deformation-induced phase transformation and the associated plasticity (TRIP effect) is caused by the strong driving force supported by the reduced stacking fault energy and increased flow stress at 77 K. The transformation mechanism from the FCC matrix to the HCP phase is revealed by transmission electron microscopy (TEM) observations. In addition to the deformation-induced phase transformation, stacking faults and dislocation slip contribute to the deformation of the FCC matrix phase at low strains and of the HCP phase at medium and large strains, suggesting dynamic strain partitioning among these two phases. The combination of TRIP and dynamic strain partitioning explain the striking strain hardening capability and resulting excellent combination of strength and ductility of iHEAs under cryogenic conditions. The current investigation thus offers guidance for the design of high-performance HEAs for cryogenic applications.

1. Introduction

High-entropy alloys (HEAs) consisting of multiple principal elements attract attention due to their excellent load carrying capacity suited for challenging structural applications [1–6]. In order to equip HEAs with high strain hardening capacity, rendering them strong and yet ductile, different deformation mechanisms were revealed and discussed. Among these, twinning-induced plasticity (TWIP) [7–14], and transformation-induced plasticity (TRIP) [15–19] have proven particularly suited in overcoming the alleged strength-ductility barrier which characterizes many metallic alloys.

One of the most representative examples of the TWIP effect in these materials has been reported for an equiatomic CoCrFeMnNi HEA, especially at low temperatures [3,7,20]. For the fine-grained CoCrFeMnNi HEA (~10 μm), the ultimate tensile strength (UTS) increases from ~600 MPa to ~1100 MP at an increase in elongation from ~45% to ~60% upon temperature reduction from 293 K to 77 K [20]. The critical resolved shear stress for twinning of this HEA is around 235 MPa, which indicates that mechanical twinning occurs already at ~7.4% true strain at 77 K and only at a much larger strain close to fracture at 293 K [20]. The strong TWIP effect thus activated at an early load stage at 77 K accounts for the simultaneous improvement of strength and ductility. On the one hand, the low probing temperature leads to a very low stacking fault energy based on *ab initio* calculations [8]. On the other hand, the flow stress is substantially higher at 77 K than at room temperature (e.g. 720 MPa vs. 420 MPa at a true strain of ~7.4) due to the temperature dependence of Peierls stress and solid solution strengthening [20,21]. As a result, mechanical twinning and the TWIP effect are significantly enhanced in the CoCrFeMnNi HEA when deformed at 77 K.

Li et al. [15] designed a TRIP non-equiatomic $Fe_{50}Mn_{30}Co_{10}Cr_{10}$ HEA with a dual-phase (DP) structure containing a face-centered cubic (FCC) matrix and hexagonal close-packed (HCP) martensite. Such a TRIP-DP-HEA exhibits an excellent combination of strength (UTS of ~850 MPa) and ductility (elongation of ~70%) at room

* Corresponding author.
** Corresponding author.
E-mail addresses: zh.wang@mpie.de (Z. Wang), zhiming.li@mpie.de (Z. Li).

https://doi.org/10.1016/j.jallcom.2018.12.061
0925-8388/

temperature. The DP structure enables a micro-composite effect and the TRIP mechanism offers high strain hardening as revealed for a wide range of microstructures obtained from different thermo-mechanical treatments [16]. Guided by *ab initio* calculations, Li et al. [17] also showed how to achieve the TRIP-DP effect in a family of five-component $Co_{20}Cr_{20}Fe_{40-x}Mn_{20}Ni_x$ (x = 0–20 at. %) HEAs via tuning the stacking fault energy through the variation of the Fe and Ni content. Likewise, Huang et al. [18] successfully enhanced the ductility in a brittle bcc $Ta_xHfZrLi$ HEA by introducing the TRIP effect. Unlike the TWIP effect, no systematic investigation on the TRIP effect in HEAs under cryogenic conditions has been conducted yet, though one of the most promising application scenarios for HEAs may lie in this field [3].

Recently, interstitial carbon has been introduced into the TRIP-DP HEA concept, and the resultant $Fe_{50}Mn_{30}Co_{10}Cr_{10}C_{0.5}$ (at. %) interstitial HEA (iHEA) shows joint activation of the TWIP and TRIP effects upon deformation at room temperature [22]. In addition to the interstitial solid solution strengthening, the carbon interstitials slightly increase the stacking fault energy (SFE) to a critical point for the present iHEA (around 18 mJ/m^2 [23]), although one should note that carbon has also been reported to decrease the SFE in some other HEAs [24]. Thus, mechanical twinning is triggered upon loading at room temperature, while the TRIP effect also remains active. In this study, we explore the deformation mechanisms of this TRIP-TWIP iHEA under cryogenic loading. The mechanical properties and underlying strain hardening mechanisms at 77 K are investigated and discussed in the light of the deformation microstructure evolution.

2. Experimental

Ingots of the $Fe_{49.5}Mn_{30}Co_{10}Cr_{10}C_{0.5}$ (at. %) iHEA were cast in a vacuum induction furnace from pure metals and carbon. The as-cast HEA blocks were hot-rolled to a thickness reduction of 50% at 900 °C and then homogenized at 1200 °C for two hours. A following thermo-mechanical treatment was performed to refine the grain size. Alloys were cold-rolled to a 60% reduction in thickness and then annealed at 900 °C for 3 min. A more detailed description of the procedures can be found in Ref. [22].

Dog-bone specimens with a gauge length of 20 mm, width of 5 mm and thickness of ~1.2 mm, were prepared for tensile tests (77 K, initial strain rate of 1×10^{-3} s^{-1}). Interrupted tensile tests to global engineering strain levels of 5% and 25% were conducted. These interrupted tensile tests, together with the complete tensile tests (tensile strains of 50% and 45% for the ~100 μm grain-sized and ~6 μm grain-sized iHEAs, respectively), enable to track the microstructure evolution at low, medium and high strains.

For examination in the scanning electron microscope (SEM), specimens were ground by silicon carbide paper and polished using a 1 μm diamond suspension, followed by final polishing using colloidal silica. Electron backscatter diffraction (EBSD) measurements were performed on a Zeiss-Crossbeam XB 1540 FIB SEM operated at 15 keV. A step size of 1 μm was used for EBSD scans of areas larger than 5000 μm^2, and all other scans were performed at a step size of 100 nm. Electron channeling contrast imaging (ECCI, ref. [25]) were examined by a Zeiss-Merlin SEM operated at 30 keV. The deformation-induced HCP phase assumes a plate shape with sizes characterized by ECCI in conjunction with the image analysis tool Image J. At least 100 measurements of HCP plate sizes were performed for each condition.

3 mm diameter disks with a thickness of ~100 μm were produced for transmission electron microscopy (TEM) examination. Disks were electropolished in an electrolyte of 5% nitric acid and 95% methanol using a Struers Tenupol 5 twin-jet electropolisher at a voltage of ~22 V with the temperature of 15 °C. The resulting thin foils were examined in a JEOL JEM-2200FS microscope operated at 200 keV under a scanning transmission electron microscope (STEM) mode. Bright field (BF), dark field (DF), selected area electron diffraction (SAD) and high resolution (HR) TEM observations were conducted in a Cs-probe corrected FEI Titan Themis 60-300 microscope operated at 300 keV.

3. Results

3.1. Starting microstructure

Fig. 1 shows the microstructures of as-homogenized and thermo-mechanically treated carbon-doped $Fe_{49.5}Mn_{30}Co_{10}Cr_{10}C_{0.5}$ (at. %) iHEAs. As shown before [15], the undoped $Fe_{50}Mn_{30}Co_{10}Cr_{10}$ (at. %) material has a FCC/HCP dual-phase structure with ~72% FCC phase fraction and ~28% HCP phase fraction [15]. When adding 0.5 at. % carbon, the HCP phase fraction is reduced to a level below 1%, and single FCC phase matrix prevails, as shown by EBSD phase and inverse pole figure (IPF) data in Fig. 1. The as-homogenized iHEA exhibits a coarse grain size of ~100 μm (Fig. 1a, referred to as CG). After cold-rolling and annealing, the average grain size refines to ~6 μm (Fig. 1c, referred to as FG). In addition, the thermo-mechanical treatment led to the formation of nano-precipitates with sizes of 50–100 nm in the FG iHEA, as shown in Fig. 1e. The chemical compositions of the nano-precipitates and the alloy matrix were probed by atom probe tomography (APT) in our previous work [22], and it revealed that these precipitates are $M_{23}C_6$ carbides with a cubic-to-cubic orientation relationship ($[100]_{FCC}||[100]_{M23C6}$ and $(100)_{FCC}||(100)_{M23C6}$) to the adjacent FCC matrix [22,26]. Very few dislocations are observed in BF STEM (Fig. 1e) and ECCI (Fig. 1f) images, suggesting that the thermo-mechanically treated iHEA is in a fully recrystallized state.

3.2. Cryogenic mechanical properties

The engineering stress-strain curves for CG and FG iHEAs at 77 K and 293 K are presented in Fig. 2a. Comparing with tensile results at room-temperature, the strength increases sharply at 77 K almost without sacrificing the ductility. When decreasing the testing temperature to 77 K, the UTS increased from ~600 MPa to ~1000 MPa for the CG iHEA and from ~900 MPa to ~1300 MPa for the FG iHEA, whereas the tensile elongations remain nearly the same for both materials.

The corresponding strain hardening rate curves for both the CG and FG iHEAs at 77 K and 293 K are displayed in Fig. 2b. The strain hardening rate curves for the fine-grained CoCrFeMnNi alloy (~17 μm) [20] and CoCrNi alloy (~16 μm) [27] at 77 K are also shown for reference. Under the cryogenic condition, the FG iHEA shows a slightly higher strain hardening rate than that of the CG iHEA at early stages of deformation (<10% strain). As strain increases, the strain hardening rates for CG and FG iHEAs are very close, due to their similar levels of phase transformation and further dynamic strain partitioning (as discussed later in section 3.3) which become the dominating deformation mechanisms in this regime as further discussed below. Normally, alloys exhibit continuously decaying strain hardening curves, i.e. the strain hardening rate continues to decrease with increasing tensile deformation, as seen for the CG and CG iHEAs at room temperature. For the CoCrFeMnNi HEA at 77 K, due to the strong TWIP effect, a rather large strain hardening plateau is observed instead. This means that a very high strain hardening rate is maintained over a surprisingly large deformation regime extending between 10% and nearly 40% true strain, i.e. until close to fracture. Interestingly, the strain hardening even increases with ongoing tensile loading for both CG and FG iHEAs at 77 K (see Fig. 2b). Comparing with the

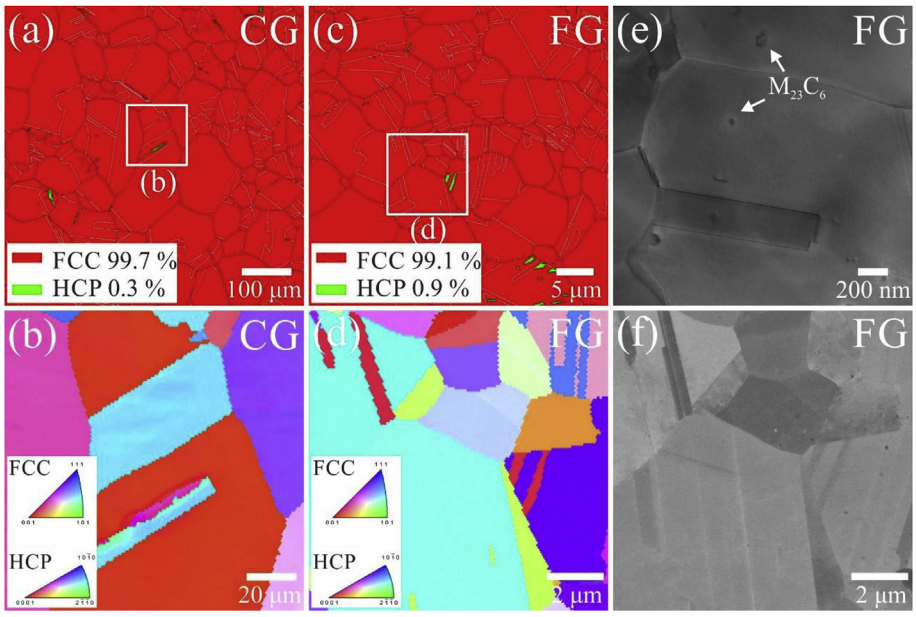

Fig. 1. Microstructures of (a–b) as-homogenized and (c–f) thermo-mechanically treated iHEAs. (a) and (c) are EBSD phase maps for the as-homogenized and recrystallized iHEAs, respectively; (b) and (d) are EBSD IPF maps corresponding to the marked regions in (a) and (c), respectively; (e) is a BF STEM image showing the existence of $M_{23}C_6$ carbides in the thermo-mechanically treated iHEA; (f) is a correlative ECC image for (d). CG refers to the as-homogenized iHEA with a coarse grain size, and FG refers to the thermo-mechanically treated iHEA with a fine grain size.

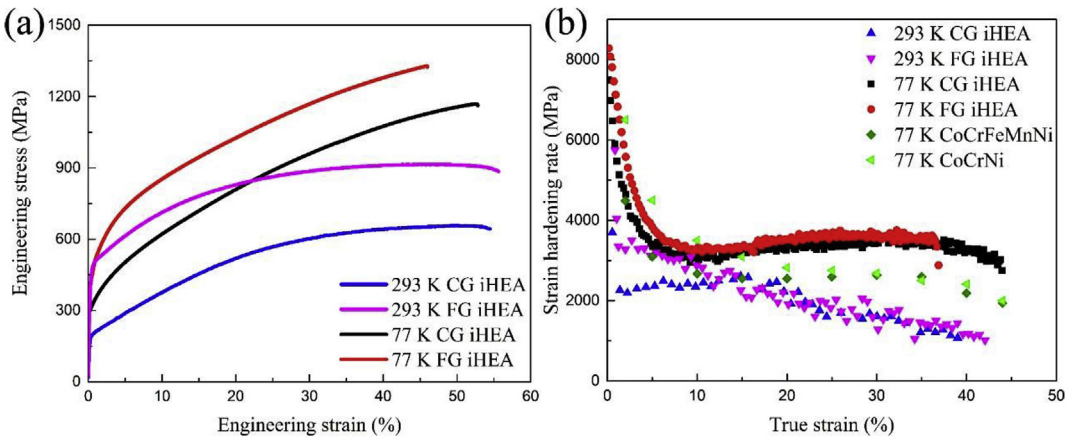

Fig. 2. (a) Engineering stress-strain curves and (b) strain hardening rate curve as a function of true strain for CG and FG iHEAs tested at 293 K and 77 K. The strain hardening rate curves for the fine-grained CoCrFeMnNi HEA (~17 μm) [20] and CoCrNi MEA (~16 μm) [27] are shown for comparison. CG and FG refer to the coarse-grained and fine-grained iHEAs, respectively.

strain hardening behavior of the CoCrFeMnNi HEA and CoCrNi MHA at 77 K, the iHEAs show significantly higher strain hardening over the entire deformation range, e.g., ~3200 MPa for the FG iHEA vs. ~2500 MPa for the CoCrFeMnNi HEA at 10% true strain and ~3800 MPa for the FG iHEA vs. ~2400 MPa for the CoCrFeMnNi HEA at 30% true strain. Even compared with the CoCrNi medium-entropy alloy (MEA), which shows very high strain hardening due to the strong TWIP effect [28], our iHEAs show significantly higher strain hardening in regimes of true strain above 15%, in which deformation-driven phase transformation and dynamic strain partitioning prevail.

3.3. Microstructures after cryogenic deformation

Fig. 3 shows EBSD phase maps for the CG and FG iHEAs at different tensile strains at 77 K. Distinct phase transformation from the FCC matrix to the HCP phase is detected upon tensile loading. The corresponding quantitative measurements of the phase fractions based on EBSD maps are shown in Fig. 4. The iHEAs contain very low fractions of HCP phase prior to tensile deformation (below 1%, Fig. 1). Due to the deformation driven phase transformation, the fraction of HCP phase increases sharply with progressing deformation. Eventually, up to 75% and 67% HCP phases are detected in the tensile-fractured CG and FG iHEAs, respectively. As depicted in Fig. 4, iHEAs tested at 77 K show much higher fraction of HCP phase than those tested at 293 K at similar strain levels, suggesting that low temperature promotes martensitic phase transformation. Interestingly, Fig. 4 also shows that at room temperature, the CG iHEA undergoes a dramatically higher fraction of phase transformation than the FG iHEA, whereas at 77 K, the deformation-driven HCP phase fractions are similar for both the CG and FG iHEAs. Owing to resolution limits, very few HCP phase regions were

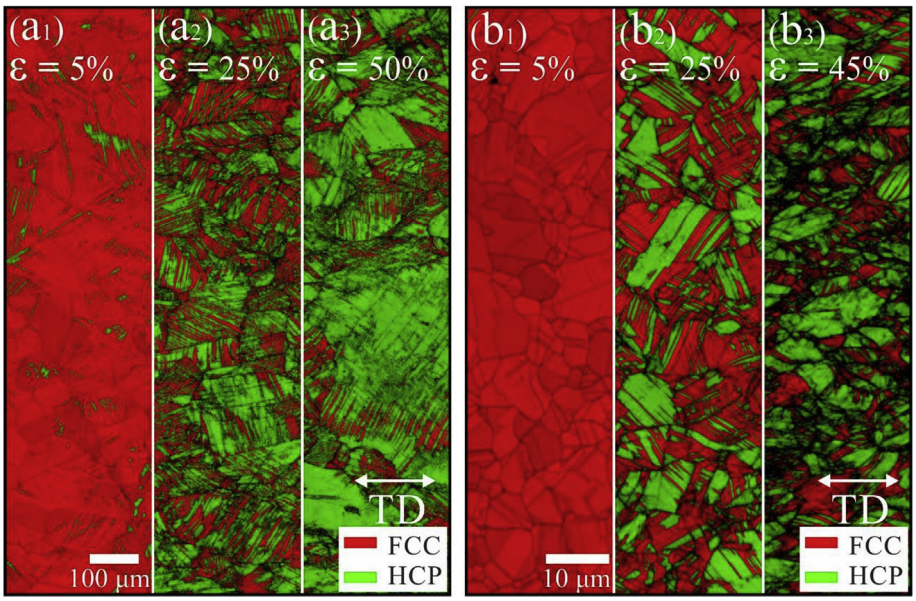

Fig. 3. EBSD maps (overlap of phase and image quality) showing the microstructure evolution for the (a) CG and (b) FG iHEAs with increasing strain levels at 77 K. CG and FG refer to the coarse-grained and fine-grained iHEAs, respectively. ε and TD refer to the global engineering strain and tensile direction, respectively.

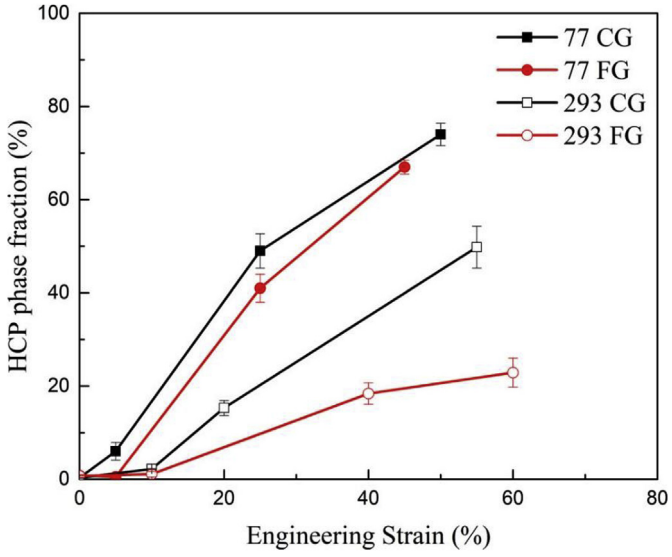

Fig. 4. HCP phase fractions of CG and FG iHEAs tested at 293 K and 77 K based on EBSD analysis. CG and FG refer to the coarse-grained and fine-grained iHEAs, respectively. Room-temperature data are taken from Ref. [22].

detected in EBSD phase maps at a low strain of 5%. Yet, multiple nano-sized HCP plates were formed already at this strain level, as observed by ECCI and TEM images.

Fig. 5 presents the microstructural evolution of the CG iHEA at different strains based on correlative EBSD and ECCI observations. At an early stage of deformation (Fig. 5a_1 - a_3), a large amount of plates with average thickness of ~80 nm are formed, a typical morphology of HCP martensite [29]. When increasing the strain to a medium level (e.g., 25%), thickening of the HCP phase occurs, with a number of new HCP plates nucleating between the existing ones, as shown in Fig. 5b_2 and b_3. Little blocks of HCP phase even appear in some areas (see Fig. 3a_2). The HCP phase becomes the dominate component in highly strained iHEA (Fig. 5c_1 and c_2). Fig. 5c_3 reveals that untransformed FCC phase regions were separated by HCP phase, which exist in the form of very thin plates.

Fig. 6 shows deformation microstructures of the 5% strained CG iHEA obtained by TEM analysis. TEM observations are consistent with the ECCI results, i.e., thick HCP plates were formed and intersected with thin HCP plates. Stacking faults (SFs) are also widely visible at such a low strain (inserted image in Fig. 6a). Due to a higher resolution of TEM relative to ECCI, dislocations are clearly seen in these BF STEM images, indicating that dislocation slip is also an essential deformation mode. The selected area diffraction (SAD) pattern in Fig. 6b confirms that these plates have the HCP structure. A typical Shoji-Nishiyama (S-N) orientation relationship, i.e., $(111)_{FCC}//(0001)_{HCP}$ and $[011]_{FCC}//[11\bar{2}0]_{HCP}$ [30], exists between the FCC matrix and the HCP phase plates, see Fig. 6b. Previous studies showed that both phase transformation and mechanical twinning occurred in the iHEAs during tensile deformation at room temperature [22]. At 77 K, however, only the deformation-induced HCP phase is seen and no mechanical twinning is observed. This is associated with the decreased stacking fault energy at lower temperature and will be discussed later.

In addition, Fig. 6 reveals the formation process of HCP plates in iHEAs tested under cryogenic conditions. Basically, HCP plates are formed through the overlapping of SFs, which is driven by the applied stress during deformation [31–33]. As seen in Fig. 6a, SFs are terminated at the interfaces of HCP plates belonging to different slip planes. These wide SFs were formed through the cross-slip of stair-rod type SFs [32], which can further overlap with each other and create HCP plates (see green arrows in Fig. 6a). Green arrows in Fig. 6c point out a different pathway to form wide SFs via cross-slip. SFs in the neighboring slip planes can readily extend once such wide SFs are formed, leading to the overlapping of these wide SFs. Also, the overlapping of wide SFs can occur via mutual interactions among dislocations, as illustrated in Fig. 6d. Slip planes in the regions adjacent to the HCP plates can be readily activated. Observations of pronounced planar dislocation slip in Fig. 6d is evident. The overlapping of SFs preferentially occurs in these places (see the green arrowed in Fig. 6d), producing HCP crystals.

The BF STEM images in Fig. 7 show deformation microstructures of the CG iHEA at strains of 25% (Fig. 7a) and 50% (Fig. 7b). More HCP plates are formed at a medium strain of 25%, accompanied by thickening of prior HCP plates. Larger blocks of HCP phase can be formed at a higher strain of 50%, as indicated by the inserted SAD

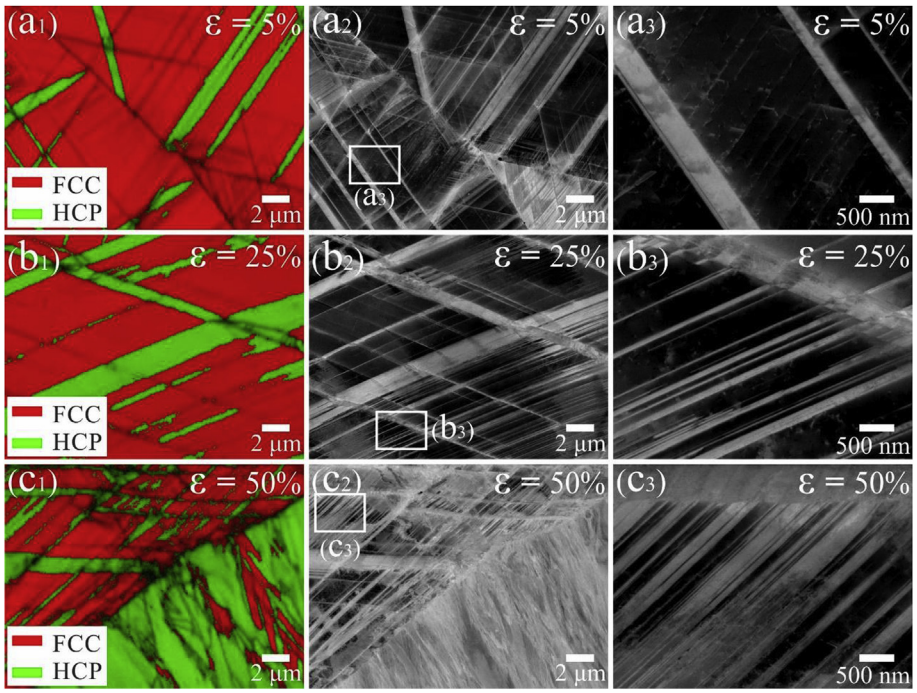

Fig. 5. EBSD maps and ECC images of the CG iHEA after (a) 5% strain, (b) 25% strain, and (c) 50% strain at 77 K. (3) shows zoom-in images for the marked regions in (2). CG refers to the coarse-grained iHEA, and ε refers to the global engineering strain.

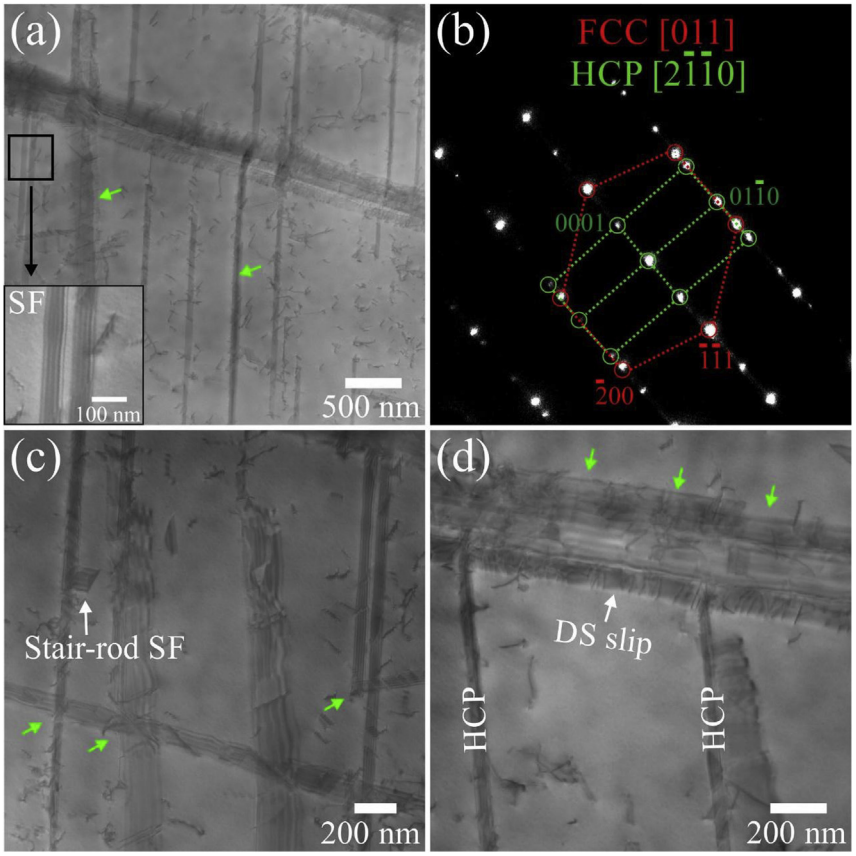

Fig. 6. BF STEM images and SAD patterns of the CG iHEA after 5% strain at 77 K. DS and SF refer to the dislocation and the stacking fault, respectively. The inserted zoom-in image in (a) shows the morphology of SF. SAD patterns in (b) are obtained under the $[011]_{FCC}$ zone axis. A Shoji-Nishiyama orientation relationship is shown between FCC and HCP phases. Green arrows indicate the formation of HCP plates through the overlapping of SFs. (For interpretation of the references to colour in this figure legend, the reader is referred to the Web version of this article.)

pattern in Fig. 7b. Fig. 7a shows that several dislocation cross-slip events and SFs are found inside the thick HCP plates. With increasing deformation, entangled dislocations with a high number density and many SFs are observed in the HCP region (see the arrowed in Fig. 7b). These dense dislocation arrays and SFs can mutually overlap in some regions. All these observations indicate that the gradually transformed HCP phase regions undergo severe deformation at later stages of tensile deformation.

The deformation microstructures obtained by the correlative EBSD and ECCI analysis for the FG iHEA at low (5%), medium (25%) and high (50%) strains are displayed in Fig. 8. Plate-shape nano-martensite phase regions are formed at low strains (Fig. 8a_1 and a_2). Their average size (~30 nm) is substantial finer than that observed in the CG iHEA (~80 nm) at the same strain. Such fine HCP plates were often not mapped by EBSD and thus, very few HCP plates were detected in Fig. 8a_1. Fig. 8a_2 shows that these thin HCP plates go through the whole grains. At a strain of 25%, frequent intersections of HCP plates were found, and new HCP plates nucleated inside the existing HCP plates (Fig. 8b_2 and b_3). Fig. 8c shows that the HCP martensite becomes the major phase, and the retained FCC phase forms very thin plates within the HCP blocks, similar to what was observed in the CG iHEA.

Fig. 9 shows the TEM/HRTEM analysis of FG iHEA at 5% strain. Very thin plates were seen in the BF TEM image (Fig. 9a). The SAD pattern shows (Fig. 9b) that these fine plates assume HCP structure, with the S-N orientation relationship to the FCC matrix. The dark field (DF) TEM image in Fig. 9b provides a clearer view on plate structures of the HCP phase. Again, no mechanical twinning is detected in the FG iHEA under deformation at 77 K. Further HRTEM analysis (Fig. 9c–e) shows that the HCP plates can be as thin as several atomic layers, i.e., formed by overlapping of stacking faults in the FCC matrix.

The effects of grain boundaries and $M_{23}C_6$ particles on dislocation movement in the FG iHEA at a low strain of 5% are shown in Fig. 10. Pile-ups of dislocations in grain boundaries and the pinning of dislocations by particles are indicted by arrows in Fig. 10a and b, respectively. These observations imply that both, grain boundaries and particles impede dislocation slip at an early stage of cryogenic deformation.

4. Discussion

4.1. Overview of the deformation behavior

A schematic drawing in Fig. 11 illustrates the cryogenic deformation behavior of CG and FG iHEAs. The iHEAs are nearly single FCC structures in undeformed state, co-existing with less than 1% fraction of the HCP phase. Upon straining, the phase transformation from the FCC matrix to the HCP martensite takes place and continues over the whole tensile deformation regime, producing a HCP phase content of ~70% in tensile-fractured CG and FG iHEAs (see Fig. 4). In addition to the martensitic phase transformation, the formation of SFs and dislocation slip are observed in both the FCC matrix and the transformed HCP phase.

At an original stage of deformation (5% strain), HCP plates are induced inside the FCC grains. Also, massive stacking faults (SFs) and planar slip of dislocations are observed in the FCC matrix. Planar slip is favored in alloys with high lattice friction stress, low stacking fault energy, and short range order [34–37]. In the present case, the high lattice friction stress, which results from the interstitial carbon, and the low stacking fault energy, evidenced by the high abundance of SFs, promote planar slip. With increasing strain, a growing number of HCP plates appear and the existing ones continue to thicken, forming large blocks of HCP phase. Except for the martensitic transformation from FCC to HCP, multiple widely extended stacking faults and tangled dislocations are found in the HCP phase at medium and high strain levels (see Fig. 7), suggesting dynamic strain partitioning among these two phases.

Unlike the deformation at room temperature, no mechanical twinning is detected during tensile loading at 77 K. Our prior studies showed the co-existence of HCP plates and mechanical twinning after 10% tensile strain [19,22]. However, in the current experiment, deformation-induced HCP phase regions were formed while no nano-twinning occurred, when the temperature decreased to 77 K, as shown by SAD probing in Figs. 6 and 9. This phenomenon is fundamentally different from observations in other FCC HEAs and MEAs, where an enhanced TWIP effect has been commonly observed at 77 K [7,20,27,38]. As noted earlier, the SFE in our current iHEA is in a critical range (around 18 mJ/m^2 [23]), which enables activation jointly of a TWIP and a TWIP effect at room temperature. The SFE decreases with reduced temperature in FCC alloys [39–42], so that at 77 K FCC-to-HCP martensitic transformation is preferential over twinning in the current iHEAs [43]. The disappearance of twinning is ascribed to the low SFE under the current cryogenic condition. Martin et al. [44] found a transition from the TWIP effect to the TRIP effect in a highly alloy CrMnNi autenitic steel when the temperature decreased from 293 K to 213 K.

4.2. Formation mechanisms of the HCP phase

SFs play a critical role in the FCC-HCP transformation, as their overlap acts as the HCP nucleation event [31,32,45,46]. TEM

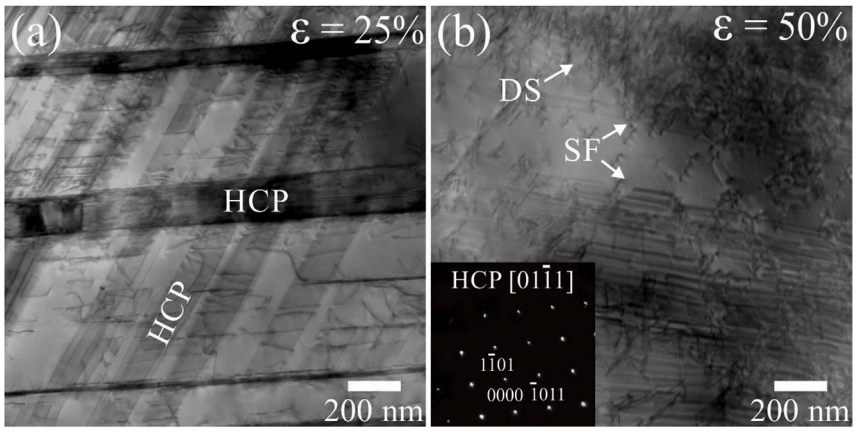

Fig. 7. BF STEM images of the CG iHEA after (a) 25% and (b) 50% strain (ε) at 77 K. DS and SF refer to dislocation and stacking fault, respectively. The inserted SAD patters in (b) indicate the whole area is a HCP structure.

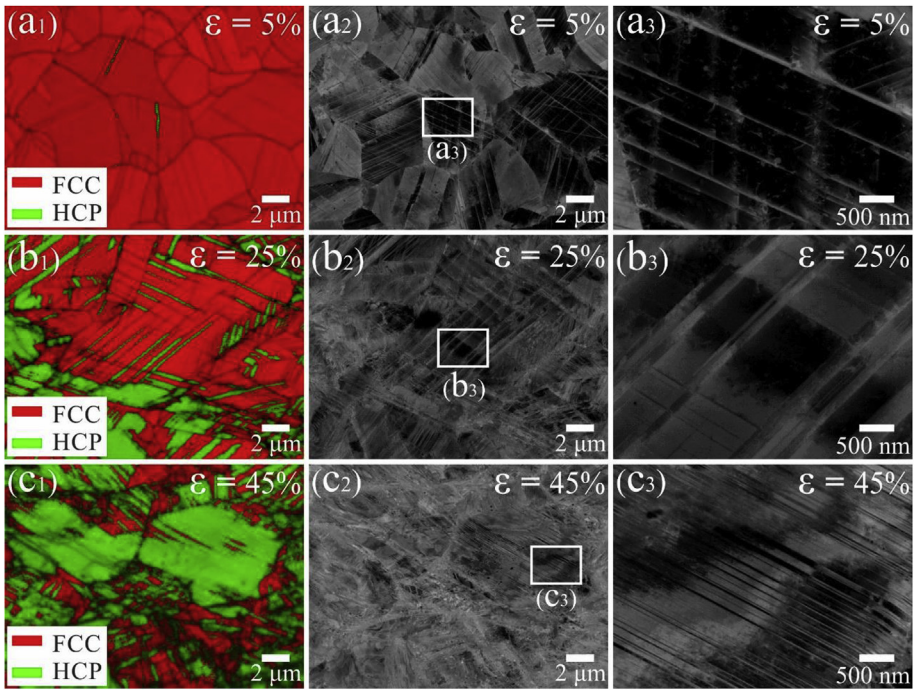

Fig. 8. EBSD maps and ECC images of the FG iHEA after (a) 5% strain, (b) 25% strain, and (c) 45% strain at 77 K. (3) shows zoom-in images for the marked regions in (2). FG refers to the fine-grained iHEA, and ε refers to the global engineering strain.

observations (Fig. 6) indicate that the HCP plates are formed following a model proposed earlier by Fujita and Ueda [32]. They suggested – as observed in the current study - that wide SFs occur via cross-slip of stair-rod type SFs or mutual interactions among dislocations. Nearby slip planes are activated during this process, and thus, SFs are more likely to extend and further overlap with each other. Our prior work [19] described the formation of HCP phase at room temperature based on Mahajan et al. [45] 's model, since it can explain the coexistence of deformation-induced twinning and HCP regions. Mahajan's approach suggests that the nucleation of six-layer HCP crystals are governed by the dislocation reaction of $\frac{a}{2}<1\bar{1}0> + \frac{a}{2}<10\bar{1}> \rightarrow 3\times\frac{a}{6}<2\bar{1}\bar{1}>$. In the present study, however, mechanical twinning does not form along with the HCP plates after deformation. In addition, the cross-slip of SFs and mutual interactions of dislocations among different slip families have been directly recorded by TEM images. These data support that, under cryogenic conditions, deformation-induced phase transformation (from the FCC matrix to the HCP martensite) in the current iHEAs is more likely to follow Fujita and Ueda's model.

Grain boundaries exert a significant influence on the morphology of HCP phase during phase transformation. Much finer HCP plates (thickness of ~30 nm) were formed in the FG iHEA than that in the CG iHEA (thickness of ~80 nm) at the initial stage of deformation (5% strain). Smaller HCP plates in the FG iHEA implies a lower growth rate of deformation-induced HCP plates. Grain boundaries have been found to hinder the growth of HCP plates and thus, phase transformation is inhibited upon grain size reduction [47–50]. In addition, interfacial back-stresses tend to raise as the grain size decreases [51], which also suppresses the growth of HCP nuclei [16]. Therefore, the HCP phase fraction is lower in the iHEA with finer grain size when testing at room temperature (see Fig. 4). Morsdorf et al. [52] reported that in Fe-0.13C-5.1Ni (wt. %) low carbon lath martensitic model alloys, materials with larger grain size also have a higher fraction of coarse martensite laths (1.5 μm in thickness).

4.3. Origin of the strain hardening under cryogenic conditions

As shown in Fig. 2b, the FG iHEA shows higher strain hardening than the CG iHEA at an early stage of deformation (<10% strain) at 77 K. TEM images in Figs. 6 and 10 reveal that dislocation slip is an essential deformation mode at this strain level. The FG iHEA has a higher fraction of grain boundaries and a fine distribution of precipitates. Both, grain boundaries and precipitates impede dislocation motions (see Fig. 10), leading to higher strain hardening.

At medium to high levels of strain, in contrast to the common decaying strain hardening curves of iHEAs tested at room temperature, cryogenic tensile tests produce increasing strain hardening. Such strain hardening behavior is attributed to the extremely high extent of deformation-driven phase transformation (up to ~70% strain-induced HCP phase for both iHEAs), and the efficient co-deformation and load-sharing between FCC and HCP, referred as dynamic strain partitioning. The latter phenomenon is essential in the current context as efficient load sharing between adjacent bulk phases works particularly well and damage-free when their compositions, elastic properties and deformation mechanisms are comparable [53,54]. These two combining deformation mechanisms also lead to a striking strain hardening capability of the current iHEAs compared to the well-established CoCrFeMnNi HEA in Fig. 2b. High and permanently maintained strain hardening delays necking, stabilizing deformation up to high strains. As a result, the strength increases sharply with only little loss in ductility, resulting in a property profile beyond the inverse strength-ductility relation when deformed under cryogenic conditions.

The key for the extraordinary strain hardening at 77 K is the very high fraction and gradual evolution of phase transformation in the iHEAs, e.g., ~67% HCP at 77 K vs. ~30% HCP at 293 K for the FG iHEAs after 50% strain. First of all, as noted above, the SFE decreases as the temperature goes down, which favors the martensitic phase transformation. In addition, the flow stress increases at 77 K, which also enhances the HCP phase transformation. A low testing temperature leads to low SFE and high flow stress, both of which

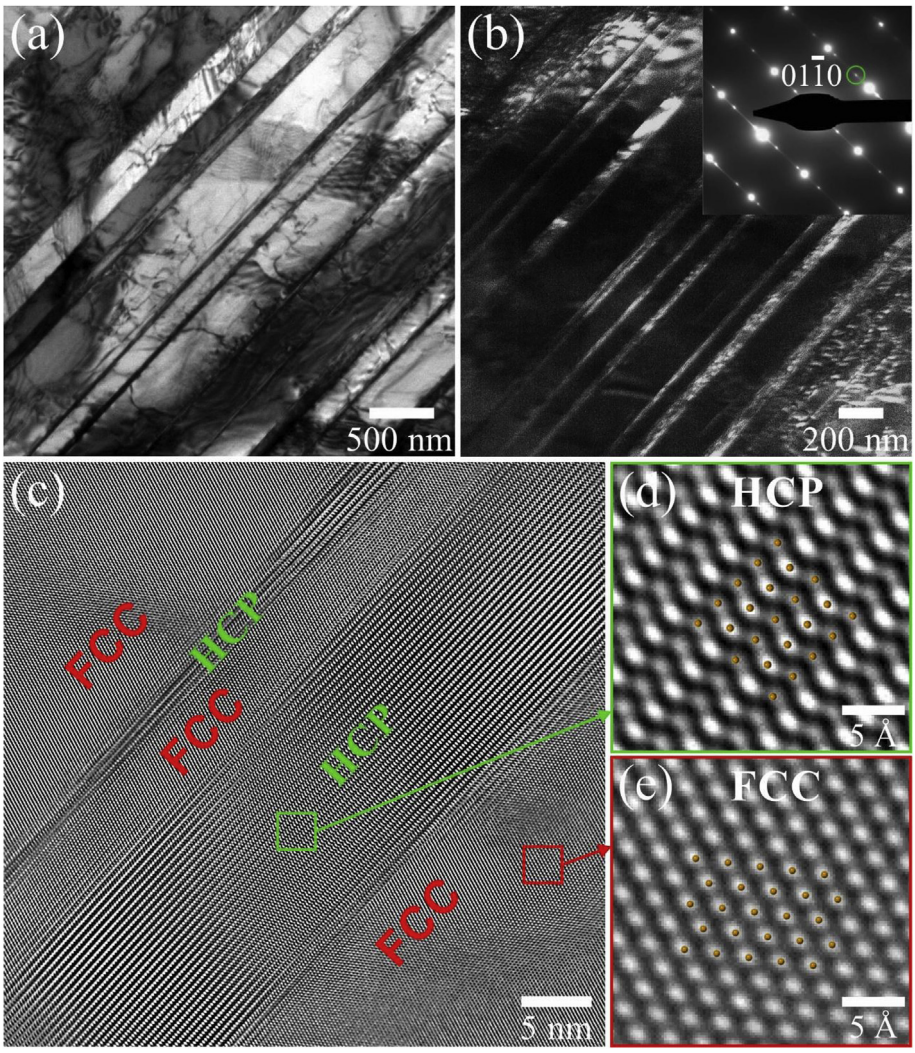

Fig. 9. (a) BF, (b) DF, and (c, d, and e) HR TEM images of the FG iHEA after 5% strain at 77 K. The DF image was taken based on the $(01\bar{1}0)$ spot, as indicated by the green circle. The HR TEM image was obtained with the electron incidence direction of $[011]_{FCC}$. (For interpretation of the references to colour in this figure legend, the reader is referred to the Web version of this article.)

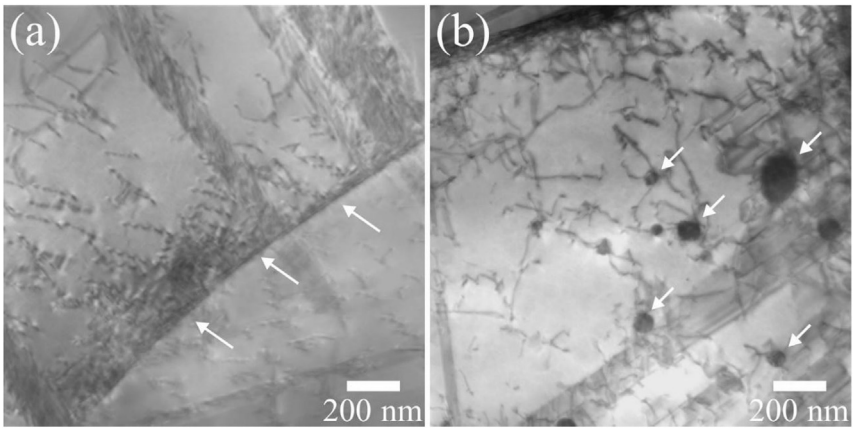

Fig. 10. BF STEM images showing the dislocations interactions with (a) grain boundaries and (b) $M_{23}C_6$ particles in the FG iHEA after 5% strain at 77 K. White arrows indicate grain boundaries and particles impede the dislocation movements.

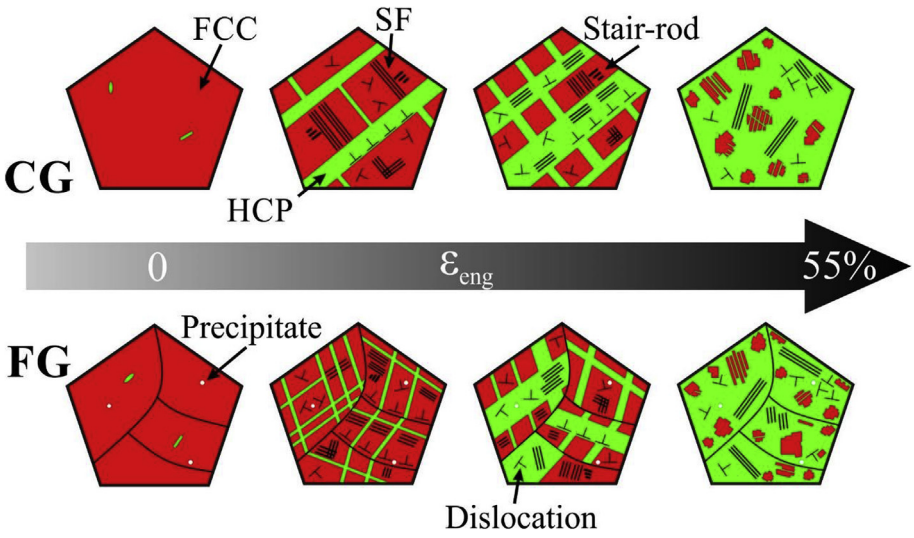

Fig. 11. A schematic drawing showing the deformation microstructure evolution of iHEAs under the cryogenic condition (77 K) at various engineering strains (ε_{eng}). CG and FG refer to the coarse-grained and fine-grained iHEAs, respectively. SF indicates the stacking fault.

significantly promote the formation of HCP phase. Similar phenomena have been also observed in Fe-22Mn-2.7Al-2.7Si-0.5C (wt. %) light-weight steel [55] and 304 L stainless steel [56,57].

It is worth noting that the CG iHEA shows a higher extent of HCP phase transformation than the FG iHEA at room temperature, whereas at 77 K, the deformation-induced HCP phase fractions are similar in both iHEAs, see Fig. 4. As previously discussed, grain boundaries are able to inhibit the HCP phase transformation, leading to a lower degree of phase transformation in the FG iHEA at room temperature. The temperature effect, however, dominates as the temperature decreases to 77 K. During deformation, the low SFE and high flow stress at such a low temperature strongly stimulate HCP transformation [57]. Consequently, up to ~70% HCP phase fraction was detected in tensile-fractured CG and FG iHEAs.

5. Conclusions

The mechanical properties and microstructure evolution of an iHEA ($Fe_{49.5}Mn_{30}Co_{10}Cr_{10}C_{0.5}$, at. %) with different grain sizes upon tensile straining under cryogenic conditions (77 K) have been investigated. The main conclusions are:

(1) The deformation-driven martensitic phase transformation rate is at a high and gradually progressing level over the whole deformation regime. In addition, at a low strain, formation of SFs and dislocations slip in the FCC phase constitute essential deformation modes. At medium to high strains, co-deformation between FCC and HCP works efficiently, i.e. constituting a highly damage-free dynamic strain partitioning behavior.
(2) HCP crystals are formed by the overlapping of wide SFs, which is a result of the cross-slip of SFs and mutual interactions among dislocations.
(3) The low SFE and high flow stress at 77 K substantially promote phase transformation from the FCC matrix to the HCP phase, resulting in a deformation-induced HCP phase fraction of up to ~70% in tensile-fractured iHEAs.
(4) The very high strain hardening at 77 K arises from the enhanced and permanently maintained TRIP effect and the dynamic stain partitioning. Such ultrahigh strain hardening further leads to the increase of strength with negligible loss of ductility, establishing metastable interstitially-doped high-entropy alloys as promising structural material class for cryogenic application scenarios.

Acknowledgements

The author Z. Wang would like to acknowledge the financial support from the Alexander von Humboldt Foundation.

References

[1] J.W. Yeh, S.K. Chen, S.J. Lin, J.Y. Gan, T.S. Chin, T.T. Shun, C.H. Tsau, S.Y. Chang, Nanostructured high-entropy alloys with multiple principal elements: novel alloy design concepts and outcomes, Adv. Eng. Mater. 6 (2004) 299–303.
[2] Y. Zhang, T.T. Zuo, Z. Tang, M.C. Gao, K.A. Dahmen, P.K. Liaw, Z.P. Lu, Microstructures and properties of high-entropy alloys, Prog. Mater. Sci. 61 (2014) 1–93.
[3] B. Gludovatz, A. Hohenwarter, D. Catoor, E.H. Chang, E.P. George, R.O. Ritchie, A fracture-resistant high-entropy alloy for cryogenic applications, Science 345 (2014) 1153–1158.
[4] Z.P. Lu, H. Wang, M.W. Chen, I. Baker, J.W. Yeh, C.T. Liu, T.G. Nieh, An assessment on the future development of high-entropy alloys: summary from a recent workshop, Intermetallics 66 (2015) 67–76.
[5] E.J. Pickering, N.G. Jones, High-entropy alloys: a critical assessment of their founding principles and future prospects, Int. Mater. Rev. 61 (2016) 183–202.
[6] D.B. Miracle, O.N. Senkov, A critical review of high entropy alloys and related concepts, Acta Mater. 122 (2017) 448–511.
[7] F. Otto, A. Dlouhý, C. Somsen, H. Bei, G. Eggeler, E.P. George, The influences of temperature and microstructure on the tensile properties of a CoCrFeMnNi high-entropy alloy, Acta Mater. 61 (2013) 5743–5755.
[8] S. Huang, W. Li, S. Lu, F. Tian, J. Shen, E. Holmström, L. Vitos, Temperature dependent stacking fault energy of FeCrCoNiMn high entropy alloy, Scr. Mater. 108 (2015) 44–47.
[9] Z. Wu, C.M. Parish, H. Bei, Nano-twin mediated plasticity in carbon-containing FeNiCoCrMn high entropy alloys, J. Alloys Compd. 647 (2015) 815–822.
[10] Y. Deng, C.C. Tasan, K.G. Pradeep, H. Springer, A. Kostka, D. Raabe, Design of a twinning-induced plasticity high entropy alloy, Acta Mater. 94 (2015) 124–133.
[11] S.W. Wu, G. Wang, J. Yi, Y.D. Jia, I. Hussain, Q.J. Zhai, P.K. Liaw, Strong grain-size effect on deformation twinning of an $Al_{0.1}$CoCrFeNi high-entropy alloy, Mater. Res. Lett. 5 (2016) 276–283.
[12] W. Abuzaid, H. Sehitoglu, Critical resolved shear stress for slip and twin nucleation in single crystalline FeNiCoCrMn high entropy alloy, Mater. Char. 129 (2017) 288–299.
[13] Y.H. Jo, S. Jung, W.M. Choi, S.S. Sohn, H.S. Kim, B.J. Lee, N.J. Kim, S. Lee, Cryogenic strength improvement by utilizing room-temperature deformation twinning in a partially recrystallized VCrMnFeCoNi high-entropy alloy, Nat. Commun. 8 (2017) 15719.
[14] W. Wu, L. Guo, B. Liu, S. Ni, Y. Liu, M. Song, Effects of torsional deformation on the microstructures and mechanical properties of a $CoCrFeNiMo_{0.15}$ high-entropy alloy, Philos. Mag. 97 (2017) 3229–3245.

[15] Z. Li, K.G. Pradeep, Y. Deng, D. Raabe, C.C. Tasan, Metastable high-entropy dual-phase alloys overcome the strength-ductility trade-off, Nature 534 (2016) 227–230.
[16] Z. Li, C.C. Tasan, K.G. Pradeep, D. Raabe, A TRIP-assisted dual-phase high-entropy alloy: grain size and phase fraction effects on deformation behavior, Acta Mater. 131 (2017) 323–335.
[17] Z. Li, F. Körmann, B. Grabowski, J. Neugebauer, D. Raabe, Ab initio assisted design of quinary dual-phase high-entropy alloys with transformation-induced plasticity, Acta Mater. 136 (2017) 262–270.
[18] H. Huang, Y. Wu, J. He, H. Wang, X. Liu, K. An, W. Wu, Z. Lu, Phase-transformation ductilization of brittle high-entropy alloys via metastability engineering, Adv. Mater. 29 (2017).
[19] M. Wang, Z. Li, D. Raabe, In-situ SEM observation of phase transformation and twinning mechanisms in an interstitial high-entropy alloy, Acta Mater. 147 (2018) 236–246.
[20] G. Laplanche, A. Kostka, O.M. Horst, G. Eggeler, E.P. George, Microstructure evolution and critical stress for twinning in the CrMnFeCoNi high-entropy alloy, Acta Mater. 118 (2016) 152–163.
[21] Z. Wu, H. Bei, G.M. Pharr, E.P. George, Temperature dependence of the mechanical properties of equiatomic solid solution alloys with face-centered cubic crystal structures, Acta Mater. 81 (2014) 428–441.
[22] Z. Li, C.C. Tasan, H. Springer, B. Gault, D. Raabe, Interstitial atoms enable joint twinning and transformation induced plasticity in strong and ductile high-entropy alloys, Sci. Rep. 7 (2017) 40704.
[23] J. Su, Z. Li, D. Raabe, Hierarchical microstructure design to tune the mechanical behavior of an interstitial TRIP-TWIP high-entropy alloy, Acta Mater. 15 (2019) 40–54.
[24] Z. Wang, I. Baker, Z. Cai, S. Chen, J.D. Poplawsky, W. Guo, The effect of interstitial carbon on the mechanical properties and dislocation substructure evolution in $Fe_{40.4}Ni_{11.3}Mn_{34.8}Al_{7.5}Cr_6$ high entropy alloys, Acta Mater. 120 (2016) 228–239.
[25] S. Zaefferer, N.-N. Elhami, Theory and application of electron channelling contrast imaging under controlled diffraction conditions, Acta Mater. 75 (2014) 20–50.
[26] Z. Li, D. Raabe, Strong and ductile non-equiatomic high-entropy alloys: design, processing, microstructure, and mechanical properties, JOM 69 (2017) 2099–2106.
[27] G. Laplanche, A. Kostka, C. Reinhart, J. Hunfeld, G. Eggeler, E.P. George, Reasons for the superior mechanical properties of medium-entropy CrCoNi compared to high-entropy CrMnFeCoNi, Acta Mater. 128 (2017) 292–303.
[28] C.E. Slone, S. Chakraborty, J. Miao, E.P. George, M.J. Mills, S.R. Niezgoda, Influence of deformation induced nanoscale twinning and FCC-HCP transformation on hardening and texture development in medium-entropy CrCoNi alloy, Acta Mater. 158 (2018) 38–52.
[29] T. Maki, Morphology and Substructure of Martensite in Steels, Phase Transformations in Steels, Woodhead Publishing, 2012, pp. 34–58.
[30] Z. Nishiyama, Crystallography of martensite, in: E.F. Morris, M. Meshii, C.M. Wayman (Eds.), Martensitic Transformation, Academic Press New York, 1978, pp. 14–134.
[31] J.A. Venables, The martensite transformation in stainless steel, Philos. Mag. 7 (1962) 35–44.
[32] H. Fujita, S. Ueda, Stacking faults and f.c.c. (γ) → h.c.p. (ε) transformation in 188-type stainless steel, Acta Metall. 20 (1972) 759–767.
[33] J.W. Brooks, M.H. Loretto, R.E. Smallman, Direct observations of martensite nuclei in stainless steel, Acta Metall. 27 (1979) 1839–1847.
[34] T. Steffens, C. Schwink, A. Korner, H.P. Karnthaler, Transmission electron microscopy study of the stacking-fault energy and dislocation structure in CuMn alloys, Philos. Mag. A 56 (1987) 161–173.
[35] V. Gerold, H.P. Karnthaler, On the origin of planar slip in f.c.c. alloys, Acta Metall. 37 (1989) 2177–2183.
[36] S.I. Hong, C. Laird, Mechanisms of slip mode modification in F.C.C. solid solutions, Acta Metall. Mater. 38 (1990) 1581–1594.
[37] I. Gutierrez-Urrutia, D. Raabe, Multistage strain hardening through dislocation substructure and twinning in a high strength and ductile weight-reduced Fe–Mn–Al–C steel, Acta Mater. 60 (2012) 5791–5802.
[38] Y. Wang, B. Liu, K. Yan, M. Wang, S. Kabra, Y.-L. Chiu, D. Dye, P.D. Lee, Y. Liu, B. Cai, Probing deformation mechanisms of a FeCoCrNi high-entropy alloy at 293 and 77 K using in situ neutron diffraction, Acta Mater. 154 (2018) 79–89.
[39] T.S. Byun, N. Hashimoto, K. Farrell, Temperature dependence of strain hardening and plastic instability behaviors in austenitic stainless steels, Acta Mater. 52 (2004) 3889–3899.
[40] S. Curtze, V.T. Kuokkala, Dependence of tensile deformation behavior of TWIP steels on stacking fault energy, temperature and strain rate, Acta Mater. 58 (2010) 5129–5141.
[41] L. Remy, Temperature variation of the intrinsic stacking fault energy of a high manganese austenitic steel, Acta Metall. 25 (1977) 173–179.
[42] L. Rémy, A. Pineau, B. Thomas, Temperature dependence of stacking fault energy in close-packed metals and alloys, Mater. Sci. Eng. 36 (1978) 47–63.
[43] S.L. Wong, M. Madivala, U. Prahl, F. Roters, D. Raabe, A crystal plasticity model for twinning- and transformation-induced plasticity, Acta Mater. 118 (2016) 140–151.
[44] S. Martin, S. Wolf, U. Martin, L. Krüger, D. Rafaja, Deformation mechanisms in austenitic TRIP/TWIP steel as a function of temperature, Metall. Mater. Trans. A 47 (2014) 49–58.
[45] S. Mahajan, M.L. Green, D. Brasen, A model for the FCC→HCP transformation, its applications, and experimental evidence, Metall. Trans. A 8 (1977) 283–293.
[46] E. Gartstein, A. Rabinkin, On the f.c.c. → h.c.p. phase transformation in high manganese-iron alloys, Acta Metall. 27 (1979) 1053–1064.
[47] S. Takaki, H. Nakatsu, Y. Tokunaga, Effects of austenite grain size on ε martensitic transformation in Fe-15mass%Mn alloy, Mater. Trans., JIM 34 (1993) 489–495.
[48] P. Huang, H.F. López, Effects of grain size on development of athermal and strain induced ε martensite in Co–Cr–Mo implant alloy, Mater. Sci. Technol. 15 (1999) 157–164.
[49] J.-E. Jin, Y.-S. Jung, Y.-K. Lee, Effect of grain size on the uniform ductility of a bulk ultrafine-grained alloy, Mater. Sci. Eng. A 449–451 (2007) 786–789.
[50] A. Kisko, R.D.K. Misra, J. Talonen, L.P. Karjalainen, The influence of grain size on the strain-induced martensite formation in tensile straining of an austenitic 15Cr–9Mn–Ni–Cu stainless steel, Mater. Sci. Eng. A 578 (2013) 408–416.
[51] C.W. Sinclair, W.J. Poole, Y. Bréchet, A model for the grain size dependent work hardening of copper, Scr. Mater. 55 (2006) 739–742.
[52] L. Morsdorf, C.C. Tasan, D. Ponge, D. Raabe, 3D structural and atomic-scale analysis of lath martensite: effect of the transformation sequence, Acta Mater. 95 (2015) 366–377.
[53] F.K. Yan, N.R. Tao, F. Archie, I. Gutierrez-Urrutia, D. Raabe, K. Lu, Deformation mechanisms in an austenitic single-phase duplex microstructured steel with nanotwinned grains, Acta Mater. 81 (2014) 487–500.
[54] C. Herrera, D. Ponge, D. Raabe, Design of a novel Mn-based 1GPa duplex stainless TRIP steel with 60% ductility by a reduction of austenite stability, Acta Mater. 59 (2011) 4653–4664.
[55] D. Raabe, C.C. Tasan, H. Springer, M. Bausch, From high-entropy alloys to high-entropy steels, Steel Res. Int. 86 (2015) 1127–1138.
[56] A.K. De, J.G. Speer, D.K. Matlock, D.C. Murdock, M.C. Mataya, R.J. Comstock, Deformation-induced phase transformation and strain hardening in type 304 austenitic stainless steel, Metall. Mater. Trans. A 37 (2006) 1875–1886.
[57] K. Spencer, M. Véron, K. Yu-Zhang, J.D. Embury, The strain induced martensite transformation in austenitic stainless steels: Part 1 – influence of temperature and strain history, Mater. Sci. Technol. 25 (2009) 7–17.